ARTICLES
https://doi.org/10.1038/s41560-019-0451-x

nature energy

Corrected: Author Correction

Continuous production of pure liquid fuel solutions via electrocatalytic CO_2 reduction using solid-electrolyte devices

Chuan Xia[1,2], Peng Zhu[1], Qiu Jiang[3], Ying Pan[2], Wentao Liang[4], Eli Stavitski[5], Husam N. Alshareef[3] and Haotian Wang[1*]

Electrocatalytic CO_2 reduction is often carried out in a solution electrolyte such as $KHCO_3$(aq), which allows for ion conduction between electrodes. Therefore, liquid products that form are in a mixture with the dissolved salts, requiring energy-intensive downstream separation. Here, we report continuous electrocatalytic conversion of CO_2 to pure liquid fuel solutions in cells that utilize solid electrolytes, where electrochemically generated cations (such as H^+) and anions (such as $HCOO^-$) are combined to form pure product solutions without mixing with other ions. Using a HCOOH-selective (Faradaic efficiencies > 90%) and easily scaled Bi catalyst at the cathode, we demonstrate production of pure HCOOH solutions with concentrations up to 12 M. We also show 100 h continuous and stable generation of 0.1 M HCOOH with negligible degradation in selectivity and activity. Production of other electrolyte-free C_{2+} liquid oxygenate solutions, including acetic acid, ethanol and *n*-propanol, are also demonstrated using a Cu catalyst. Finally, we show that our CO_2 reduction cell with solid electrolytes can be modified to suit other, more complex practical applications.

Electrocatalytic CO_2 reduction reaction (CO_2RR) to form valuable liquid fuels using renewable energy is a potential strategy to achieve a carbon-neutral energy cycle[1–4]. Exciting progress has been achieved over the past decade in developing and understanding a variety of catalytic materials for synthesis of different liquid fuels, C_1 to C_3 products such as formic acid (HCOOH)[5–8], ethanol[9–11] and *n*-propanol[12,13]. These liquid products were usually generated and mixed with solutes in the electrolyte of traditional H- or flow-cell reactors, which requires extra separation and concentration processes to recover pure liquid fuel solutions in practical applications[14,15]. Taking CO_2RR to HCOOH as a representative example, while highly selective (>90%) and active catalysts have been presented in recent works[16–22], in most cases the products were actually in the form of formate due to the neutral or alkaline electrolyte environments, as well as in low concentrations. Similarly, production of electrolyte-free C_{2+} liquid oxygenate solutions is still an open challenge. Therefore, to directly and continuously produce pure liquid fuel solutions, particularly with high product concentrations and long-term operation, is highly desired for the practical deployment of electrocatalytic CO_2RR.

Solid-state batteries recently emerged as promising alternatives to traditional solution electrolyte batteries, where ions are shuttled between anode and cathode via ion-conducting solid polymers or ceramics for better reliability[23,24]. Inspired by this battery chemistry, here we sought to employ a solid-state electrolyte (SSE) in a CO_2RR system to produce electrolyte-free liquid products including HCOOH, acetic acid, ethanol and *n*-propanol. In contrast to the dissolved solutes (such as the commonly used $KHCO_3$) in a conventional liquid electrolyte, these solid ion conductors help to transport electrogenerated cations or anions (protons or formates in the case of HCOOH) to form pure products, avoiding mixture with solutes as in the case of a conventional liquid electrolyte. Therefore, once coupled with highly selective CO_2RR catalysts, this design could enable a continuous production of ultrahigh-purity liquid fuel solutions. Since HCOOH is the only liquid product that has been produced exclusively by CO_2RR, we first use it as an ideal candidate for the demonstration of pure liquid fuel solutions via electrocatalytic CO_2RR using solid electrolytes. A high concentration of 12.1 M pure HCOOH solution, as well as a 100 h continuous and stable generation of ~0.1 M HCOOH, was successfully demonstrated. Following the same mechanism, other types of electrolyte-free liquid fuel including C_2 and C_3 products were also demonstrated when changing the catalysts.

Cell configuration

As schematically illustrated in Fig. 1, the cathode and anode of the proposed cell are catalyst-coated gas diffusion layer (GDL) electrodes, which were separated by anion and cation exchange membranes (AEM and CEM), respectively. Porous solid ion conductors, for example proton (H^+) or formate ($HCOO^-$) conductors, were placed in between the membranes with close contact to efficiently transport the generated ions and significantly minimize the ohmic loss of the entire device. Similar three-chamber designs using strong acids or strong acid cation exchange media in the middle chamber for both ion conduction and pure product collection have been demonstrated before[6,25], but the versatility of solid electrolytes needs to be further expanded for different application scenarios. The solid electrolyte in this work was made of ion-conducting polymers with different functional groups, such as porous styrene–divinylbenzene copolymer consisting of sulfonic acid functional groups for H^+

[1]Department of Chemical and Biomolecular Engineering, Rice University, Houston, TX, USA. [2]Rowland Institute, Harvard University, Cambridge, MA, USA. [3]Materials Science and Engineering, King Abdullah University of Science and Technology (KAUST), Thuwal, Saudi Arabia. [4]Kostas Advanced Nanocharacterization Facility (KANCF), Northeastern University, Innovation Campus at Burlington, MA (ICBM), Burlington, MA, USA. [5]National Synchrotron Light Source II, Brookhaven National Laboratory, Upton, NY, USA. *e-mail: htwang@rice.edu

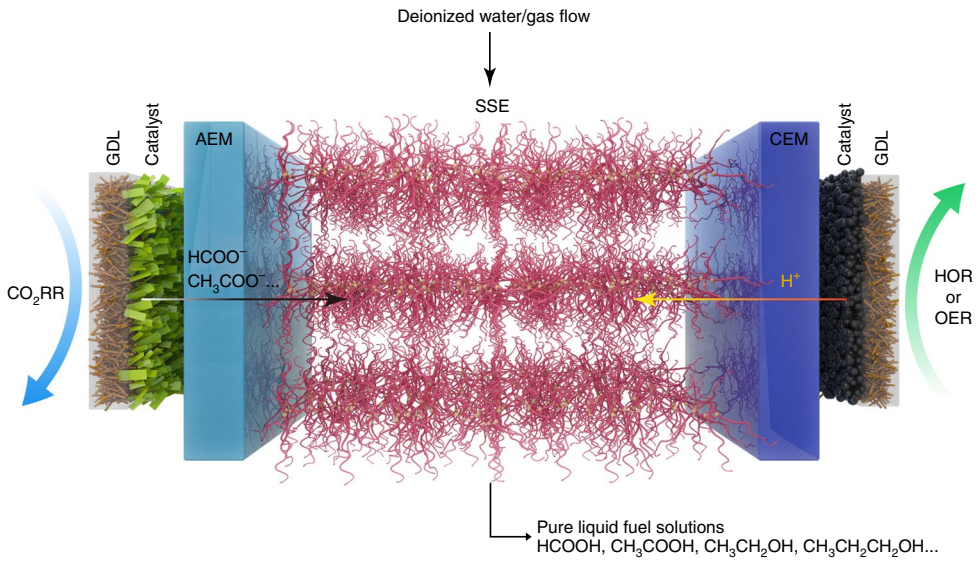

Fig. 1 | Schematic illustration of the CO_2 reduction cell with solid electrolyte. The SSE is either an anion or cation conductor. Depending on the type of solid ion-conducting electrolyte in between, the HCOOH product could be formed via the ionic recombination of crossed ions at either the left (H^+-conductor) or right ($HCOO^-$-conductor) interface between the middle channel and membrane, and diffuse away through the liquid water.

conduction, or quaternary amino functional groups for $HCOO^-$ conduction. An inorganic solid proton conductor, $Cs_xH_{3-x}PW_{12}O_{40}$, was also demonstrated. Other forms of solid electrolyte used in batteries, such as ceramics, polymer/ceramic hybrids or solidified gel electrolytes (for example 10 wt% H_3PO_4/polyvinylpyrrolidone gel), could also be employed in the future.

In our design, the cathode electrode where CO_2 is reduced was supplied with humidified CO_2 gas to facilitate CO_2 mass transport, whereas the anode side was circulated with 0.5 M H_2SO_4 solution for water oxidation. The flooding issue of the GDL electrode, usually in direct contact with water, is a common concern for traditional H- or flow-cell reactors that blocks CO_2 diffusion and thus significantly limits their CO_2RR lifespan[6,16,21,26–30]. Of note, the cathode GDL in this current design is completely separated from liquid media, which, in principle, guarantees its stability even when operated under large negative overpotentials for high catalytic currents[31–33]. When CO_2 is reduced by a HCOOH-selective catalyst, the generated negatively charged $HCOO^-$ driven by the electrical field travels through the AEM towards the middle solid-electrolyte channel. At the same time, protons generated by water oxidation on the anode side can move across the CEM to compensate the charge. Depending on the type of solid ion-conducting electrolyte in between, the HCOOH product could be formed via the ionic recombination of crossed ions at either the left (H^+-conductor) or right ($HCOO^-$-conductor) interface between the middle channel and membrane, as depicted in Fig. 1, and diffuse away through the liquid water. Then, the formed liquid products can be quickly released by the slow deionized water stream or humidified inert gas flow. Obviously, pure HCOOH solution with a wide range of concentrations can be produced by adjusting the flow rate of the deionized water and gas.

Synthesis of a two-dimensional Bi catalyst

A variety of HCOOH-selective electrocatalysts, such as Bi, Co, Pd, In, Pb, Sn and carbonaceous material, could be coupled into this proposed CO_2RR system for pure HCOOH solution generation[22,34–39]. Among them, Bi-based catalysts have achieved peak Faradaic efficiencies (FEs) of over 95% at high current densities (>50 mA cm^{-2}), outperforming most other non-noble-metal catalysts[16,17,21,40,41]. This is because CO_2 reduction to formate was the most energetically favourable among the competing cathodic processes on the Bi surface[17]. However, large overpotentials were usually required to drive significant CO_2RR currents, which leads to low energy conversion efficiencies. More importantly, the Bi-based electrocatalysts in previous reports usually involve multistep or complicated synthesis methods, making low-cost and large-scale productions in the future difficult.

Here, we develop a facile and scalable hydrolysis approach, followed by in situ electrochemical reduction to synthesize an ultrathin two-dimensional Bi (2D-Bi) catalyst for CO_2-to-HCOOH conversion, which thereby presents abundant undercoordinated active Bi sites for significantly improved catalytic performance. Due to the simplicity of our synthesis method, kilogram-scale synthesis of this Bi catalyst has been demonstrated in our laboratory using a 1 l reactor (Supplementary Fig. 1a). Specifically, commercial bismuth nitrate was first hydrolysed to form layered basic bismuth nitrate—$Bi_6O_6(OH)_3(NO_3)_3$•$1.5H_2O$ (BOON)—which was then topotactically converted into 2D-Bi by in situ electroreduction. During the hydrolysis step, cetyltrimethylammonium bromide (CTAB) was used as a surface capping agent to obtain ultrathin 2D-BOON. Br^- ions have been demonstrated to suppress the stacking of monolayers for Bi compounds during bottom-up synthesis, and the extra surface repulsion from the hydrophobic long chains of CTA^+ ions could further terminate the stacking of layered basic bismuth nitrates[42]. The X-ray diffraction pattern reveals the phase purity of the tetragonal basic bismuth nitrates (Supplementary Fig. 1b). The BOON crystal structure is based on cationic $[Bi_2O_2]^{2+}$ layers in the (a, b) plane (Supplementary Fig. 1a). In the interlayer space, two layers of anions are inserted: one is composed of OH^- groups and the other of NO_3^- (ref. [43]). The hydrogen bonds between the two negative layers (OH^-•••NO_3^-) further increase the cohesion of the structure.

Scanning electron microscopy (SEM) and aberration-corrected transmission electron microscopy (TEM) images (Fig. 2a,b and Supplementary Fig. 2a–e) showed few-layer-thick BOON nanosheets with good homogeneity. Notably, the nanosheets were almost transparent to the electron beam, suggesting their ultrathin feature. The lattice spacing in the high-resolution TEM image was measured to be 0.288 nm (Fig. 2c), corresponding to the (006) planes

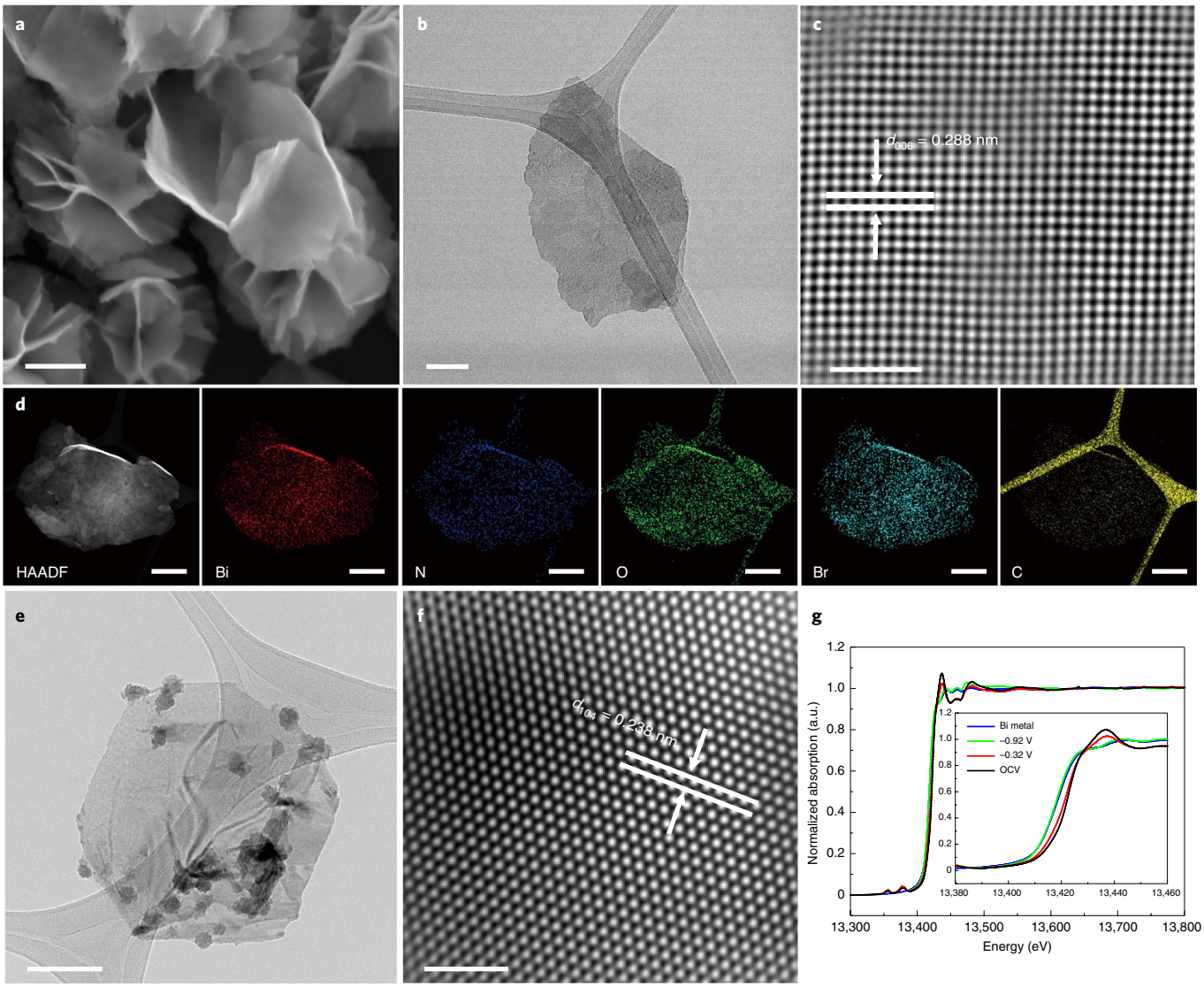

Fig. 2 | Characterization of BOON and 2D-Bi. a–c, SEM (**a**), TEM (**b**) and high-resolution TEM (**c**) of the BOON nanosheet with arrows highlighting the (006) interplanar distance. **d**, STEM-EDS elemental mapping of BOON. HAADF, high-angle annular dark field. **e**,**f**, TEM (**e**) and high-resolution TEM (**f**) of in situ reduced metallic 2D-Bi with arrows highlighting the (104) interplanar distance. **g**, In operando Bi L_3-edge XAS spectra of BOON at different potentials during electrocatalytic CO_2RR. Inset: the X-ray absorption near-edge spectroscopy region of the spectra. OCV, open circuit voltage. Commercial Bi was used as a reference. Note that the potentials in **g** are not current × resistance (*iR*) compensated. Scale bars: **a**, 500 nm; **b**,**e**, 100 nm; **d**, 300 nm; **c**,**f**, 2 nm.

of tetragonal BOON. In addition, the corresponding fast Fourier transform analysis of an individual BOON nanosheet indicated its quasi-single-crystalline nature (Supplementary Fig. 2f). Scanning transmission electron microscopy–energy dispersive spectroscopy (STEM-EDS) elemental mapping (Fig. 2d) showed a uniform distribution of Bi, O, N, C and Br in the BOON nanosheet, confirming the CTAB capping effect. The BOON nanosheets were then electrochemically reduced to 2D-Bi metal in CO_2-saturated 0.5 M $KHCO_3$ solution. X-ray diffraction measurement of the reduced material showed obvious diffraction peaks assignable to metallic Bi (Supplementary Fig. 1c), consistent with the X-ray photoelectron spectroscopy analysis (Supplementary Fig. 1d). The X-ray photoelectron spectroscopy and STEM-EDS studies also demonstrated the absence of Br at the Bi surface (Supplementary Fig. 1,e,f), suggesting the formation of clean metallic Bi. It is worth noting that the in situ formed Bi metal still retains the original nanosheet morphology of BOON (Fig. 2e). The lattice spacing in Fig. 2f is 0.238 nm, which agrees well with the (104) interplanar spacing in rhombohedral Bi. The thickness of an individual Bi nanosheet determined by atomic force microscopy was only a few nanometres (<5 nm, Supplementary Fig. 3a), revealing its 2D nature with maximally exposed surface sites. It is also interesting that our process yields 2D-Bi with quasi-single-crystal nature (Supplementary Fig. 3b), which could benefit in-plane electron transportation. In addition, we showed that about 59.8% of the Bi sites of 2D-Bi were electrochemically active using cyclic voltammetry (Supplementary Fig. 3c). This high percentage could ensure a high Bi atom efficiency during CO_2RR catalysis[18].

In operando X-ray absorption spectroscopy (XAS) can help to elucidate the electronic structure change of our Bi catalyst under reaction conditions[32]. Figure 2g shows the in situ Bi L_3-edge normalized absorption spectra at different applied potentials, as well as commercial Bi metal as a reference. We observed a negative energy shift of the Bi edge from open circuit voltage to −0.32 V versus the reversible hydrogen electrode (RHE), suggesting the reduction of Bi oxidation states. With the negative potential further increased to

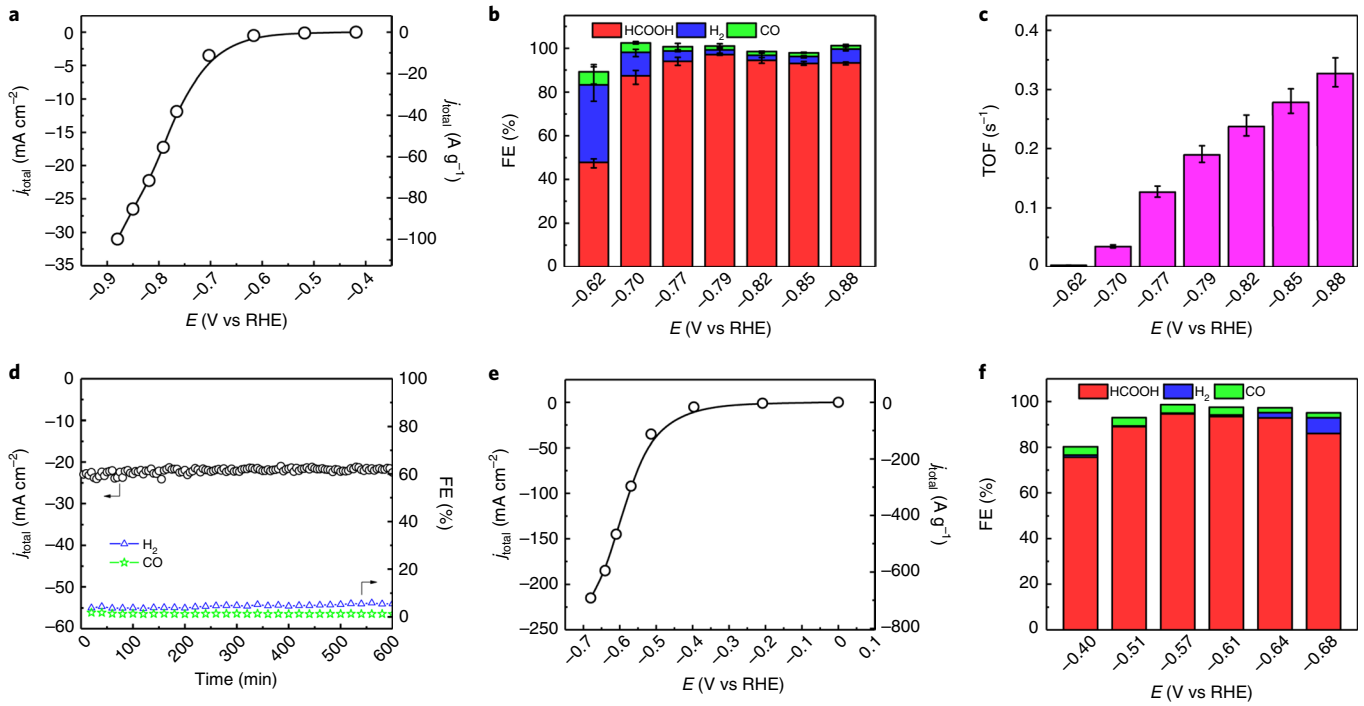

Fig. 3 | Electrocatalytic CO_2 reduction to formate using the 2D-Bi catalyst. a, The overall current density of the 2D-Bi in the H-type cell. **b**, FE of each CO_2 reduction product on 2D-Bi at different potentials *E*. The error bars represent the s.d. calculated from three independent samples. **c**, The TOF of 2D-Bi in an H-cell test. Note that the surface active Bi sites were estimated using a cycling voltammetry study. **d**, Chronoamperometric stability test at −0.83 V versus RHE in an H cell for 10 h, which indicates an average formate FE of about 96.5% estimated from NMR. **e**,**f**, The overall current density of the 2D-Bi on a GDL in a flow-cell system (**e**), and the corresponding FEs of the resultant reduction products (**f**).

−0.92 V, the Bi L_3-edge spectra overlapped with the metallic Bi reference, which indicated that the active phase under CO_2RR conditions was metallic.

CO_2-to-formate performance of the 2D-Bi catalyst

The CO_2RR catalytic activity of 2D-Bi was first evaluated in CO_2-saturated 0.5 M $KHCO_3$ aqueous electrolyte (pH = 7.4) in a standard three-electrode H-cell system (Methods). Gas and liquid products were separately analysed using gas chromatography (GC) and nuclear magnetic resonace (NMR), respectively. As expected, formate was the only liquid product, together with a small amount of CO and H_2. The maximal formate FE can reach about 99% with a partial current density (j_{HCOO^-}) of 17.3 mA cm^{-2} (55.7 A g^{-1}) at −0.79 V versus RHE (Fig. 3a,b). High formate FEs (>90%) can still be maintained with negative potentials further increased, reaching a partial current of ~30 mA cm^{-2} at an overpotential of only 710 mV. A CO_2-to-formate Tafel slope of 121 mV per decade on 2D-Bi (Supplementary Fig. 4a) was obtained, which is very close to 118 mV per decade, indicating that an initial electron transfer rate might be the determining step during CO_2RR[44]. The formate production turnover frequency (TOF) per active Bi site can be estimated via the electrochemically active Bi/Bi^{3+} redox reaction[17]. As shown in Fig. 3c, the TOF of 2D-Bi was calculated to be 0.19 and 0.33 s^{-1} at overpotentials of 620 (99% formate FE) and 710 mV (93% formate FE), respectively. This 2D-Bi catalyst can be continuously operated in an H cell at a constant potential of −0.83 V to maintain a 10 h stable cathodic current of 21 mA cm^{-2} with an average formate FE of 96.5%, suggesting its remarkable stability for long-term operations, which will be further demonstrated below. Postcatalysis SEM characterization reveals that the 2D-Bi nanosheet structure is well maintained (Supplementary Fig. 4b–d), which explains its high average formate selectivity. However, a tiny amount of microscale Bi, potentially formed from Bi atom reconstruction under reaction conditions in water, was observed on the catalyst surface and could lead to the slightly increased H_2 evolution with time. The 2D-Bi CO_2RR catalytic performance can be further boosted with a GDL electrode to facilitate the CO_2 mass transport in a traditional flow cell[16,45,46]. Following an early onset of a mere 227 mV, the peak formate FE of 95% was achieved at −0.57 V versus RHE with a current density of 92 mA cm^{-2} (Fig. 3e,f). Impressively, over 200 mA cm^{-2} current with a high formate selectivity of 86.1% requires only 510 mV overpotential, suggesting an efficient energy conversion process. Due to its ultrathin nature, this layered catalyst reached a CO_2-to-formate specific activity of 583.9 A g^{-1}, indicating a high Bi atom efficiency.

Production of pure liquid fuels

The excellent CO_2RR performance of the 2D-Bi catalyst as well as its easy scalability therefore make good preparations for the demonstration of producing pure HCOOH solution in our proposed CO_2 reduction cell with solid electrolytes. IrO_2–C on the anode side was selected as a very stable and active oxygen evolution reaction (OER) catalyst in acidic solutions[47], which helps to release H^+ from water to compensate for the negative charges of the generated $HCOO^-$ (Fig. 1). Figure 4a plots the CO_2RR activity of a 2D-Bi//solid-electrolyte//IrO_2–C cell with different types of solid ion conductor. In the case of an H^+ conductor the overall current density can reach over 100 mA cm^{-2} at a cell voltage of 3.27 V, while the $HCOO^-$ conductor delivers a lower current of 50 mA cm^{-2} at about 3.47 V. No liquid products were observed other than HCOOH by ^{1}H and ^{13}C NMR (Supplementary Fig. 5). In the cell with the H^+-conducting solid electrolyte, a peak HCOOH FE of 93.1% with a partial current of 32.1 mA cm^{-2} was achieved at 3.08 V (Fig. 4b), corresponding to 0.112 M pure HCOOH solution at a deionized water flow rate of 12 ml h^{-1} (with electrode geometric area of 4 cm^2). The pH of this produced HCOOH solution was measured to be about 2.3–2.4, which agrees well with the theoretical pH value of

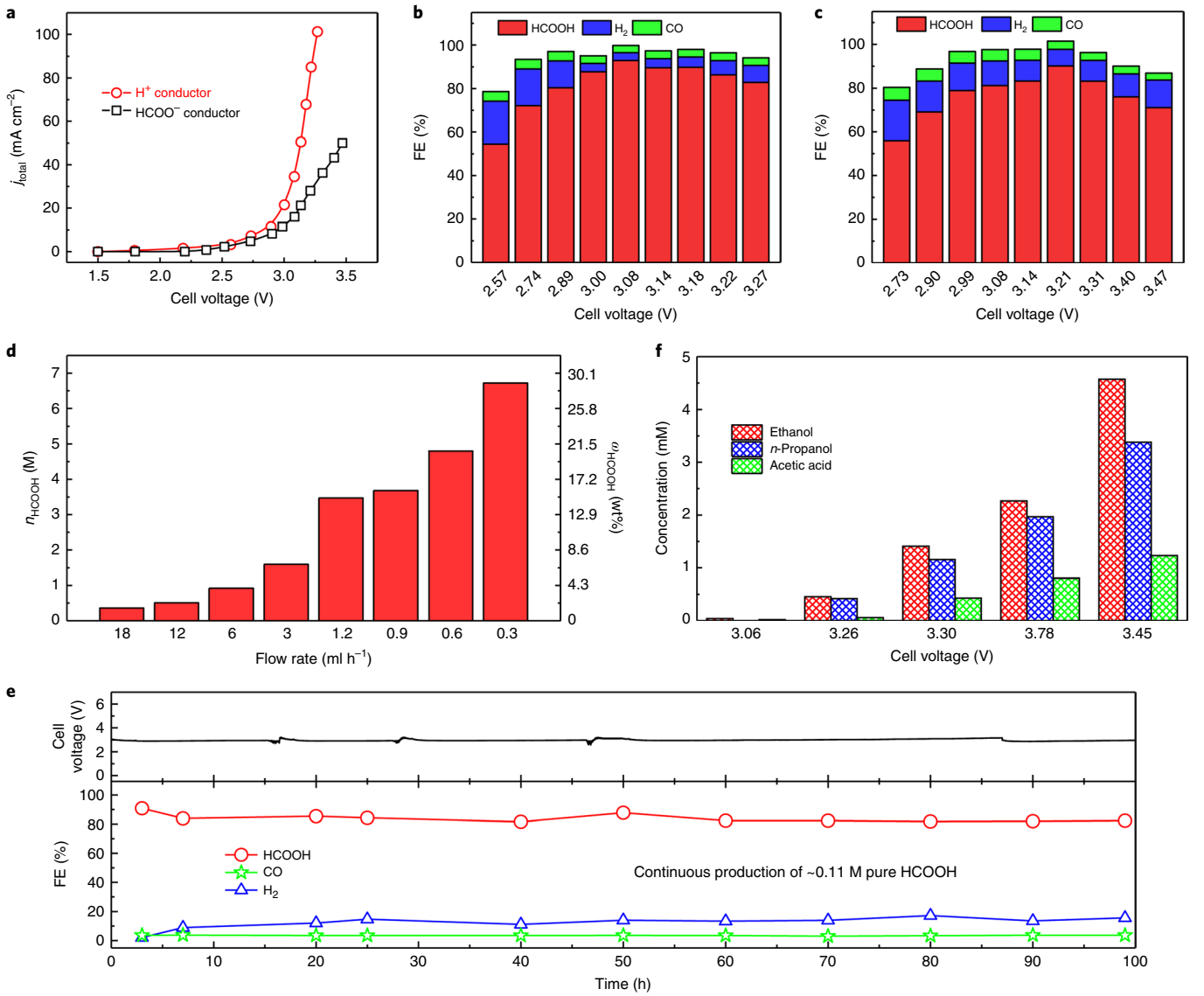

Fig. 4 | Production of pure liquid fuels using CO_2 reduction system with solid electrolyte. a, The current densities against cell voltages on a 2D-Bi catalyst using our CO_2 reduction system with H^+ and $HCOO^-$ conducting solid electrolytes. **b**,**c**, The corresponding FEs for the reduction products at different cell voltages using H^+ (**b**) and $HCOO^-$ (**c**) conducting solid electrolyte. **d**, The dependence of HCOOH concentration on the deionized water flow rate maintaining an overall current density of 100 mA cm^{-2}, indicating that concentrated pure HCOOH solution (up to 6.73 M) can be continuously produced. **e**, Long-term operation test of CO_2 reduction to pure HCOOH solution showing high selectivity stability of our 2D-Bi catalyst at 30 mA cm^{-2} using this proposed CO_2 reduction system with H^+ conductor. The FE of HCOOH is maintained at more than 80% over the 100 h continuous operation. **f**, Production of electrolyte-free C_{2+} liquid fuel solutions using commercial Cu_2O catalyst, showing that small-molecular oxygenate liquid fuels can also be efficiently collected.

0.112 M pure HCOOH solution (pH = 2.36). Furthermore, negligible amounts of impurity ions including potassium, sodium, iron, bismuth, sulfur (all lower than 100 ppm) and iridium (lower than 10 ppb) were detected by inductively coupled plasma atomic emission spectroscopy (ICP-OES). The pH and ICP-OES results, taken together, demonstrate the ultrahigh purity of the HCOOH solution produced by our device. Under this maximal HCOOH selectivity, an impressive energy conversion efficiency of 42.3% from electricity to pure HCOOH was delivered.

In addition, a similar peak HCOOH FE of 90.1% with a HCOOH partial current of 28 mA cm^{-2} was obtained at 3.21 V using a $HCOO^-$ conductor (Fig. 4c), demonstrating the generality of our SSE concept for pure HCOOH solution production. Importantly, we show that the concentration of pure HCOOH solution can be easily controlled by tuning the flow rate of the deionized water stream (Fig. 4d). By slowing down the deionized water flow, higher HCOOH concentration of 6.73 M (~29 wt%) was achieved in CO_2-to-HCOOH conversion using H^+ conductor with an FE of 30% (Supplementary Fig. 6). The decreased HCOOH FEs with increased HCOOH concentrations might be due to two factors. First, the concentrated HCOOH solution in the solid-electrolyte channel may thermodynamically lower the CO_2-to-HCOOH conversion rate. Second, it can cross the Nafion film and be oxidized by the anode, which has been typically observed in direct formate fuel cells[48]. We found that if Nafion 1110 CEM (254 μm thick) was used instead of Nafion 117 (183 μm thick) we could achieve higher HCOOH FE. Specifically, we obtained the HCOOH FE of 40.3% at 100 mA cm^{-2} and 0.6 ml h^{-1} deionized water rate for Nafion 117, while 51.1% HCOOH FE is achieved for Nafion 1110 under the same conditions. It is also worthwhile to note that the improvement of HCOOH FE is still limited even when thicker

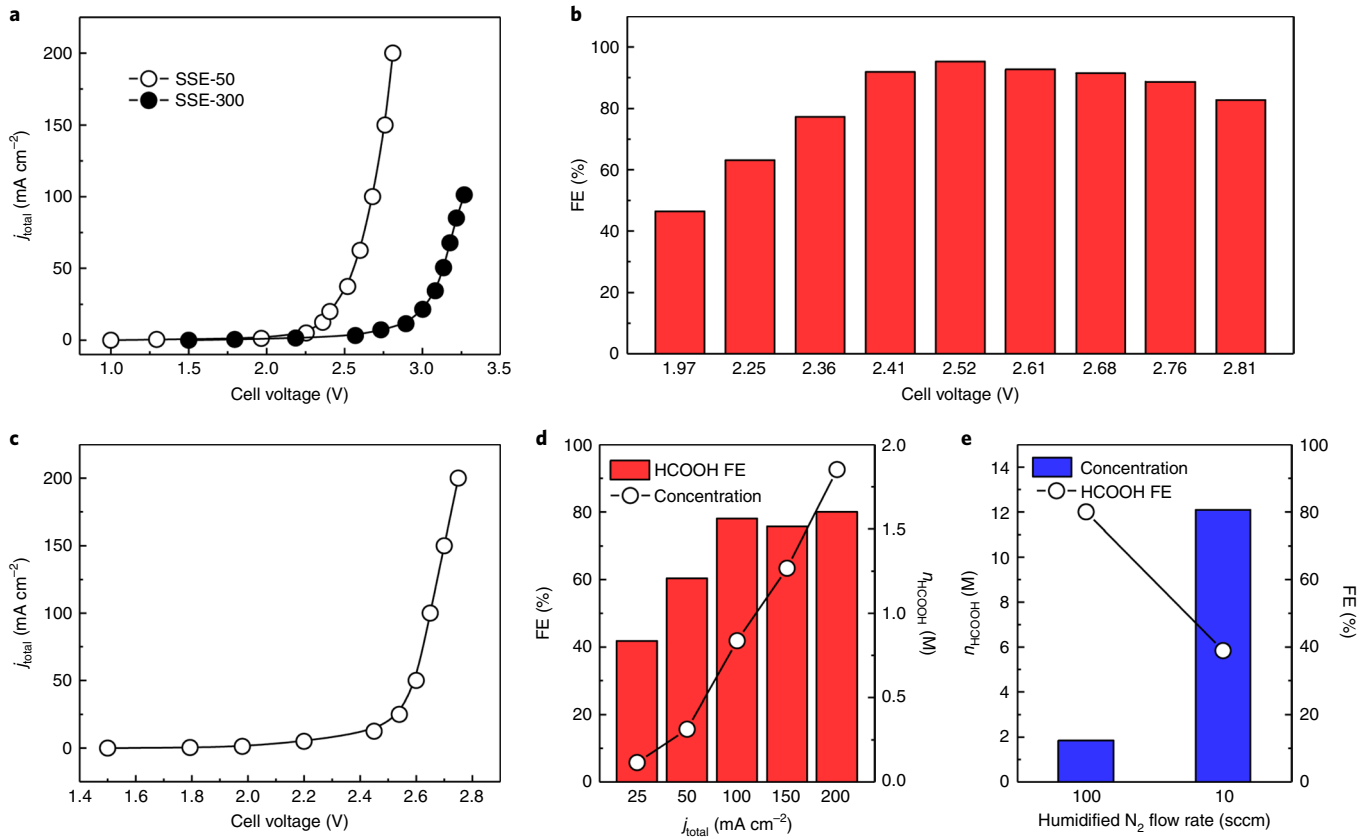

Fig. 5 | Production of pure HCOOH solution and vapour using optimized CO_2 reduction system with solid electrolyte. a, The current densities against cell voltages on a 2D-Bi catalyst using our CO_2 reduction system with SSE-50 or with SSE-300 H^+ conducting solid electrolyte. **b**, The corresponding FEs for the reduction products at different cell voltages. The value shown is the mean calculated from two independent samples. **c**, The current densities against cell voltages on a 2D-Bi catalyst where 100 sccm humidified N_2 flow was used to extract the formed HCOOH from the SSE-50 solid-electrolyte layer. **d**, The corresponding HCOOH FEs and concentrations at different applied current densities. **e**, The dependence of HCOOH concentration on the N_2 gas flow rate, maintaining an overall current density of 200 mA cm^{-2}, indicating that concentrated pure HCOOH solution (up to 12.1 M) can be continuously produced.

CEM (254 versus 183 μm) is employed to block the HCOOH from crossing. Thus, we believe that the concentrated HCOOH solution in the solid-electrolyte layer also thermodynamically lowers the CO_2-to-HCOOH conversion rate.

A 100 h continuous and stable production of ~0.11 M pure HCOOH solution was demonstrated using our 2D-Bi catalyst in this solid-electrolyte CO_2RR cell (Fig. 4e). The current density was fixed at 30 mA cm^{-2} (120 mA cell current) and the deionized water flow rate at 16.2 ml h^{-1}, resulting in a total of 1.6 litre 0.1 M pure HCOOH product (Supplementary Fig. 7a). Over this 100 h course the cell voltage showed negligible change, and the HCOOH selectivity was maintained above 80%. The water contact angle test reveals the superhydrophobicity of the 100 h aged cathode GDL (Supplementary Fig. 7b,c), demonstrating that no water flooding occurred. SEM characterization of the post-stability catalyst reveals no Bi particulate agglomerates (Supplementary Fig. 7d), further highlighting the advantages of our cell configuration for long-term stability compared with the H-cell. We also note that a higher-concentration HCOOH solution (for example >1.0 M) can be stably and continuously obtained (Supplementary Fig. 7e). Analysis of the HCOOH in the generated concentrate HCOOH solution (150 mA cell current, 2 ml h^{-1} deionized water flow for 20 h) leads to an average HCOOH FE of about 80.9%, translating to ~1.13 M HCOOH. In addition, besides the polymer solid electrolyte, we showed that an inorganic solid proton conductor, such as insoluble $Cs_xH_{3-x}PW_{12}O_{40}$, can also be employed for pure HCOOH generation (Methods and Supplementary Fig. 8), significantly expanding the application range of solid-electrolyte design.

Based on the same working mechanism, other types of electrolyte-free CO_2RR liquid product can be obtained using this solid-electrolyte cell design. To demonstrate its wide applicability for other pure liquid fuel productions beyond HCOOH, we therefore chose Cu catalyst, which can generate multiple C_{2+} oxygenate fuels[11,49]. Based on the Cu catalyst derived from commercial Cu_2O nanoparticles, we show that electrolyte-free dense C_{2+} oxygenate fuels, including ethanol, acetic acid and *n*-propanol, can be efficiently collected (Fig. 4f). At 3.45 V, we obtained an electrolyte-free oxygenate solution containing 4.6 mM ethanol, 3.4 mM *n*-propanol and 1.3 mM acetic acid. The GC and NMR results present an overall approximately 100% FE (Supplementary Fig. 9a,b), indicating that all the generated liquid fuels have been successfully collected by the deionized water stream. The above discussion confirms that the solid-electrolyte cell design can be easily extended to produce other pure liquid fuels such as pure ethanol solutions once a highly selective and exclusive CO_2RR catalyst is developed.

While the pure HCOOH solution has been demonstrated using our SSE design, the relatively low cell energy efficiency at high production rate—about 36% at the current density of 100 mA cm^{-2}—needs to be further improved. We sought to optimize the proton solid electrolyte to decrease the required cell voltage for pure HCOOH production. The polymer proton conductor we used has an average domain size of about 300 μm, which was

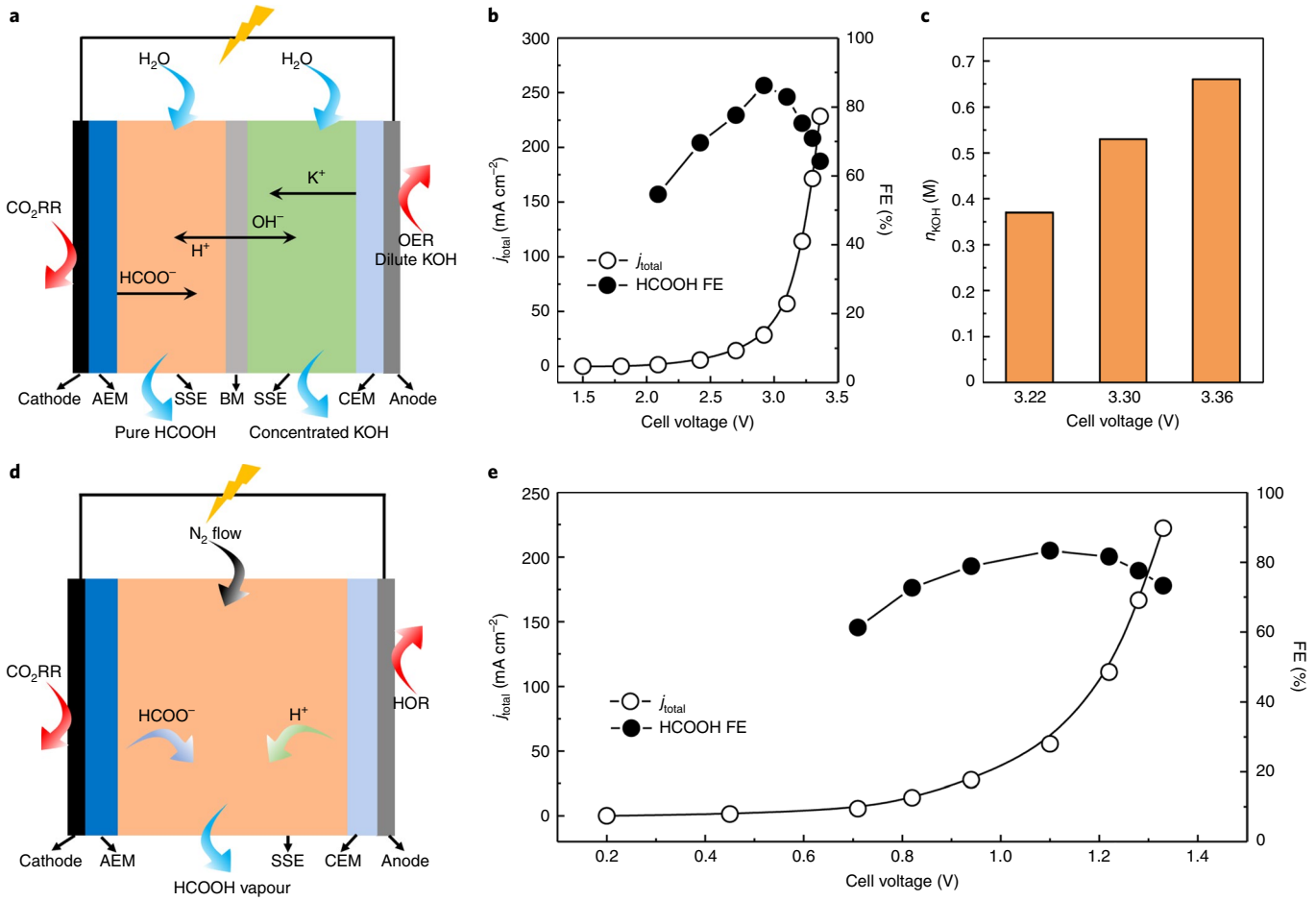

Fig. 6 | Different CO_2RR system with solid electrolyte for more complex practical applications. a, Schematic illustration of the proposed four-chamber CO_2 reduction cell with solid electrolyte. BM represents the bipolar membrane. Yellow and green SSE layers represent highly porous SSE-50 and SSE-OH^-, respectively. **b**, The current densities against cell voltages of a 2D-Bi//SSE-50 | bipolar | SSE-OH^-// NiFe-LDH cell (Methods), and the corresponding HCOOH FEs. **c**, The concentration of pure KOH, which is simultaneously produced using the four-chamber solid cell during CO_2 reduction. **d**, Schematic illustration of the proposed all-solid-state cell for direct CO_2 hydrogenation. SSE is the highly porous SSE-50 proton solid conductor. **e**, The current densities and the corresponding HCOOH FEs against cell voltages on a 2D-Bi//Pt-C all-solid-state cell using the SSE-50 H^+ conducting solid electrolyte. The generated pure HCOOH vapour was brought out from the middle solid electrolyte using 100 sccm humified N_2.

further decreased to ~50 μm (henceforth referred to SSE-300 and SSE-50, respectively) for higher porosity and ion conductivity. As shown in Supplementary Fig. 10, the SSE-50 offers higher ionic conductivity (0.018 S cm^{-1}) and lower charge transfer (12.5 Ω cm^2) resistivity compared with SSE-300 (0.0064 S cm^{-1} and 24.5 Ω cm^2), due to the improved surface area and porosity. Figure 5a compares the CO_2RR activity of a 2D-Bi//IrO_2-C cell using polymer proton ion conductors. In the case of highly porous solid electrolyte (SSE-50), the overall current density can quickly ramp up to 200 mA cm^{-2} (4 cm^2 geometric area) with a high HCOOH FE of 82.7% (Fig. 5b), outperforming SSE-300. As a result, we achieved an improved energy efficiency of about 48.5% and 43.3% at the current density of 100 and 200 mA cm^{-2}, respectively. Such an improvement suggests that the overall performance of CO_2-to-fuel conversion can be further boosted in the future by improving the ionic conductivity of the solid electrolyte. With these high current densities and selectivity, the maximal one-pass efficiency for CO_2 conversion is calculated as about 23% (20 sccm CO_2 feed-in rate) at a HCOOH partial current density of 165.4 mA cm^{-2} (Supplementary Fig. 11). The 2D-Bi//SSE-50//IrO_2-C cell also demonstrated continuous and stable production of pure HCOOH solution with no degradations in activity or selectivity (Supplementary Fig. 12a), suggesting good stability as a result of using highly porous SSE in our system.

We also show that more concentrated HCOOH could be obtained when using humidified inert gas instead of deionized water flow to bring out the generated liquid fuel vapour followed by cold condensation. Figure 5c exhibits the recorded current–voltage curve of a 2D-Bi//SSE-50//IrO_2-C cell with 100 sccm humidified N_2 gas passed through the middle solid-electrolyte layer. Despite the different trapping media (deionized water or gas flow) within the porous solid electrolyte, the overall catalytic activities and selectivities (Fig. 5a–d) are similar, which implies good stability of the solid conductor and catalytic reactor. Specifically, the HCOOH FE using N_2 flow at 2.75 V (200 mA cm^{-2}) is 80.1%, which is very close to that using deionized water (82.7% at 2.81 V, 200 mA cm^{-2}), but the concentration of generated HCOOH (for example 0.84 M at 100 mA cm^{-2}) was higher than that using a deionized water stream at a flow rate of 16.2 ml h^{-1} (for example. 0.55 M at 100 mA cm^{-2}). When the N_2 gas flow was slowed down from 100 to 10 sccm, we obtained a high HCOOH concentration of 12.1 M (~49.3 wt%) by electrocatalytic CO_2 reduction (Fig. 5e), which is beneficial, technically and economically, for practical applications, for example a direct formic acid fuel cell where concentrated HCOOH is preferred[50]. Furthermore, a quantitative techno-economic analysis of our entire device demonstrates that the proposed method for CO_2-to-HCOOH conversion using

2D-Bi and SSE is highly competitive with current commercial technologies (Supplementary Note 1).

Upgraded solid-electrolyte device

Generation of protons by water oxidation on the anode side is indispensable to produce pure formic acid using the above proposed solid electrocatalytic cell. However, electrocatalytic water oxidation in acidic solution is challenging. Only noble metal catalysts such as IrO_2 or RuO_2 could offer modest performance. To exclude the costly OER catalyst (IrO_2 in our case) and make our strategy more economically appealing, we further upgrade our solid electrocatalytic cell into a symmetric four-chamber configuration to simultaneously produce three kinds of high-purity product, in which the alkaline/neutral solution can be used for OER. In this case, nickel iron layered double hydroxide (NiFe-LDH)[51] and 0.1 M KOH were chosen as the OER catalyst and electrolyte to decrease the catalyst cost and anode overpotential. As schematically illustrated in Fig. 6a, AEM and CEM were also used to separate catalyst-coated GDLs and the porous SSE-50 solid ion conductors. A bipolar membrane was employed to separate the cathode and anode compartments, which dissociates water into H^+ and OH^- during CO_2 reduction[52]. The generated H^+ ions from the bipolar membrane can neutralize the negatively charged $HCOO^-$ in the left solid-electrolyte layer to produce pure HCOOH. At the same time, more concentrated KOH can be obtained in the right solid-electrolyte layer via ionic recombination of OH^- and K^+. The experimentally measured current–voltage profile and the corresponding HCOOH FE of this four-chamber cell is presented in Fig. 6b. A peak HCOOH partial current of about 150 mA cm^{-2} could be achieved at 3.36 V. More importantly, we successfully collected the pure KOH solution of concentration up to 0.66 M at a deionized water flow rate of 16.2 ml h^{-1} (Fig. 6c), demonstrating the feasibility of our strategy. Furthermore, we performed a 20 h stability test on this four-chamber reactor (Supplementary Fig. 12b). Impressively, the cell performance showed no obvious changes during the course of the stability test. In future applications, brine streams could be used as an anolyte to drive the chlorine evolution at the anode side to replace the OER. Then, three kinds of valuable pure product (HCOOH, NaOH and Cl_2) could be simultaneously generated. Implementation of NaOH, Cl_2 and HCOOH production from a brine stream and CO_2 using our solid-electrolyte concept can offer environmentally sound, economic strategies for sustainable desalination and carbon cycling.

Coupling OER with CO_2RR for HCOOH production will lead to O_2 byproduct, which results in lower 'atom economy' ($2CO_2 + 2H_2O \rightarrow 2HCOOH + O_2$), as well as involving aqueous electrolyte. Hence, we also explored electrocatalytic hydrogenation of CO_2 using H_2 as a feedstock at the anode towards pure HCOOH vapour under ambient conditions without any liquid stream involved. As schematically illustrated in Fig. 6d, hydrogen was electrochemically oxidized into protons at the anode, which is catalysed by commercial Pt/C, whereas the CO_2 is reduced into formate at the cathode using the 2D-Bi. The electroreduced $HCOO^-$ ions will combine with the generated protons, which cross from the hydrogen oxidation reaction (HOR) side, to form pure HCOOH. Then, the formed HCOOH vapour at the solid-electrolyte surface will be extracted by the continuous humified N_2 flow. Of note, no liquid stream was required for the entire cell, leading to an all-vapour-phase operation. This solid-electrolyte electrochemical cell can offer a 100% atom utilization without byproducts for HCOOH production using CO_2 and H_2 as feedstocks ($CO_2 + H_2 \rightarrow HCOOH$). Figure 6e displays the current–voltage profile of the direct electrocatalytic CO_2 hydrogenation cell for HCOOH vapour generation. A peak HCOOH FE of 83.3% was obtained at only 1.1 V. An impressive HCOOH partial current of about 163 mA cm^{-2} (HCOOH FE of 73.3%) can be achieved at the low cell voltage of a mere 1.33 V. It is important to mention that the formed HCOOH can be detected at as low as 0.45 V, translating to a small cell overpotential of only 0.26 V. We have also presented the continuous generation of HCOOH vapour using our vapour phase reactor for 20 h (Supplementary Fig. 12c), demonstrating the good stability of the catalyst and solid ion conductor over a long operation period. This electrocatalytic CO_2 hydrogenation to HCOOH vapour under ambient conditions presents advantages over traditional thermocatalytic CO_2 hydrogenation processes, which usually involve high temperature and pressure.

Conclusions

We have demonstrated an approach to electrocatalytic CO_2 reduction that uses a solid-electrolyte design that can generate pure liquid product solutions or vapours. Given the wide variety of solid electrolytes available, we expect that the approach could be extended to production of other liquid fuels as well as to other electrocatalytic reactions. We also demonstrate a facile hydrolysis method for large-scale synthesis of an active, selective and stable 2D-Bi catalyst for CO_2-to-HCOOH conversion catalysts. Future work will be focused on catalytic materials design for exclusive C_{2+} liquid fuel production. Moreover, further improvements in ion conductivity and stability of the solid electrolyte will significantly increase the energy efficiency of the electrosynthetic cell.

Methods

Preparation of BOON nanosheet. In a typical gram-scale synthesis, 970 mg $Bi(NO_3)_2 \cdot 5H_2O$ was first dissolved in 60 ml deionized water, followed by the addition of 500 mg CTAB. Then, 3.0 g urea was added to 40 mL ethanol to form a homogeneous solution using sonication. Next, the urea–ethanol solution was quickly added to the $Bi(NO_3)_2$ aqueous solution, and the mixture was stirred for 30 min to form a white homogeneous solution. This homogeneous solution was finally kept at 90 °C in a water bath for 4 h. The resultant white BOON nanosheets were collected by centrifugation, washed with deionized water and alcohol, and dried at 60 °C.

Preparation of the 2D-Bi catalyst. Typically, 10 mg of as-prepared BOON powder was mixed with 2 ml of ethanol and 40 µl of binder solution (Nafion 117 (Sigma-Aldrich, 5%) for H and flow cells and alkaline ionomer (Dioxide Materials, 5%) for the proposed new cell), and sonicated for 20 min to obtain a homogeneous ink. 160 µl of the ink was pipetted onto 2 cm^2 glassy carbon surface (0.4 mg cm^{-2} mass loading), and vacuum dried before usage. Then, the BOON-loaded glassy carbon electrode was electroreduced at −1.6 V versus saturated calomel electrode (SCE) in CO_2-saturated 0.5 M $KHCO_3$ solution (pH = 7.4) for 10 min to obtain black 2D-Bi catalyst. For the conventional flow cell and the cell with solid electrolyte, a 0.4 mg cm^{-2} BOON-nanosheet-loaded gas diffusion electrode (Sigracet BC 35, Fuel Cell Store) was electroreduced at −1.6 V versus SCE in CO_2-saturated 0.5 M $KHCO_3$ solution for 10 min, and then washed using deionized water to obtain the 2D-Bi catalyst for CO_2RR.

Preparation of NiFe-LDH catalyst. The NiFe-LDH catalyst for OER was prepared according to a previous report[51].

Electrocatalytic CO_2 reduction. The electrochemical measurements were run at 25 °C in a customized gas-tight H-type glass cell separated by Nafion 117 membrane (Fuel Cell Store). A Bio-Logic VMP3 workstation was employed to record the electrochemical response. In a typical three-electrode system, a platinum foil (Beantown Chemical, 99.99%) and an SCE (CH Instruments) were used as the counter- and reference electrode, respectively. The as-prepared 2D-Bi on glassy (0.4 mg cm^{-2}) was used as the working electrode. The backside of glassy carbon was covered by an electrochemically inert, hydrophobic wax (Apiezon wax WW100) during electrochemical tests. All potentials measured against SCE were converted to the RHE scale in this work using $E_{RHE} = E_{SCE} + 0.244\,V + 0.0591\,pH$, where pH values of electrolytes were determined with an Orion 320 PerpHecT LogR Meter (Thermo Scientific). CO_2-saturated 0.5 M $KHCO_3$ aqueous solution was used as the electrolyte in our study with a pH of 7.4. The electrolyte in the cathodic compartment was stirred at a rate of 1,000 r.p.m. during electrolysis. Solution resistance (R_s) was determined by potentiostatic electrochemical impedance spectroscopy at frequencies ranging from 0.1 Hz to 200 kHz. All the measured potentials were manually compensated unless stated otherwise.

For the conventional flow-cell test, 0.4 mg cm^{-2} 2D-Bi-loaded Sigracet 35 BC GDL electrodes (Fuel Cell Store) was used as the CO_2RR cathode. An IrO_2/C electrode (Fuel Cell Store) was used as the anode for water oxidation. The two electrodes were therefore placed on opposite sides of two 0.5-cm-thick polytetrafluoroethylene sheets with 0.5 cm wide by 2.0 cm long channels such

that the catalyst layer interfaced with the flowing liquid electrolyte.[46] A Nafion film was sandwiched by the two polytetrafluoroethylene sheets to separate the chambers. The geometric surface area of the catalyst is 1 cm^2. On the cathode side a titanium gas flow chamber supplied 20 sccm CO_2 while the anode was open to the atmosphere. The flow rate of 2.0 M KOH electrolyte (pH = 14.2) was 30 ml h^{-1} in both chambers controlled by a syringe pump. A SCE was used as the reference electrode.

For the cell with solid electrolyte, a PSMIM AEM[53–55] (Dioxide Materials) and a Nafion film (Fuel Cell Store) were used for anion and cation exchange, respectively. A Sigracet 35 BC GDL electrode loaded with 0.4 mg cm^{-2} 2D-Bi (4 cm^2 electrode area) and an IrO_2/C electrode (Fuel Cell Store) were used as cathode and anode, respectively. The cathode was supplied with 20 sccm of humidified CO_2 gas, and the anode was circulated with 0.5 M H_2SO_4 aqueous solution at 2 ml min^{-1}. The porous (~300 µm; SSE-300) and highly porous (~50 µm, SSE-50) styrene–divinylbenzene sulfonated copolymer[56] was used as the solid H^+ conductor. The insoluble solid acid $Cs_xH_{3-x}PW_{12}O_{40}$[57] was used as the inorganic H^+ conductor. The porous solid Dowex 1 × 4 copolymer was employed as the $HCOO^-$ and OH^- conductor (Sigma). The 2D-Bi//SSE//IrO_2-C cell was first stabilized for 120 min before liquid product collection. For the four-chamber cell, 0.4 mg cm^{-2} 2D-Bi- and NiFe-LDH-loaded Sigracet 35 BC GDL electrodes (4 cm^2 electrode area) were used as cathode and anode, respectively. The cathode was supplied with 20 sccm of humidified CO_2 gas, and the anode was circulated with 0.1 M KOH aqueous solution at 2 ml min^{-1}. A bipolar membrane (Fuel Cell Store) was used to separate the anode and cathode reactions. The above-mentioned H^+ conductor (SSE-50) and porous OH^- conductor (SSE-OH^-) were used as the solid electrolyte filling in between the cathode and membrane and between the anode and membrane, respectively. For the CO_2RR//SSE//HOR cell, 0.4 mg cm^{-2} 2D-Bi- and Pt-C (Fuel Cell Store)-loaded Sigracet 35 BC GDL electrodes (4 cm^2 electrode area) were used as cathode and anode, respectively. The SSE-50 H^+ conductor was used as the solid electrolyte. 100 sccm humified N_2 was used to bring out the formed HCOOH vapour.

To quantify the gas products during electrolysis, CO_2 gas (Airgas, 99.995%) was delivered into the cathodic compartment at a rate of 20.0 sccm (monitored by an Alicat Scientific mass flow controller) and vented into a gas chromatograph (Shimadzu GC-2014) equipped with a combination of molecular sieve 5A, HayeSep Q, HayeSep T and HayeSep N columns. A thermal conductivity detector was mainly used to quantify H_2 concentration, and a flame ionization detector with a methanizer was used to quantitatively analyse the content of CO and/or any alkane species. The partial current density for produced gas product was calculated as

$$j_i = x_i v \frac{n_i F p^o}{RT} (\text{electrode area})^{-1}$$

where x_i is the volume fraction of a certain product determined by online GC referenced to calibration curves from the standard gas sample (Airgas), v is the flow rate of 20 sccm, n_i is the number of electrons involved, $p^o = 101.3$ kPa, F is the Faradaic constant, $T = 298$ K and R is the gas constant. The corresponding FE at each potential is calculated as $\frac{j_i}{j_{overall}} \times 100$.

One-dimensional ^{1}H NMR spectra were collected on an Agilent DD2 600 MHz spectrometer to test if any liquid products were present during the CO_2 reduction over the 2D-Bi catalyst. Typically, 600 µl of electrolyte after electrolysis was mixed with 100 µl of D_2O (Sigma-Aldrich, 99.9 at.% D) and 0.05 µl dimethyl sulfoxide (Sigma-Aldrich, 99.9%) as internal standard. ^{13}C NMR spectra were acquired using a 500 MHz SB Liquild Bruker Avance NMR spectrometer at room temperature to check the purity of the as-prepared HCOOH solution. Typically, 500 µl of electrolyte after electrolysis was mixed with 60 µl of D_2O (Sigma-Aldrich, 99.9 at.% D).

The energy efficiency is calculated using the following equations:

$$\text{energy efficiency} = \frac{E_{OER} - E_{CO_2\text{-to-HCOOH}}}{E_{cell}} \text{FE}_{HCOOH}$$

where E_{OER} (1.23 V versus RHE)[58] and $E_{CO_2\text{-to-HCOOH}}$ (−0.17 versus RHE)[59] are the theoretical potential for OER and CO_2 reduction to HCOOH, respectively. E_{cell} is the required cell voltage.

Characterization. Powder X-ray diffraction data were collected using a Bruker D2 PHASER diffractometer in parallel beam geometry employing Cu Kα radiation (wavelength 1.54056 Å) and a one-dimensional LYNXEYE detector, at a scan speed of 0.02° per step and a holding time of 1 s per step. X-ray photoelectron spectroscopy was carried out with a Thermo Scientific K-Alpha ESCA spectrometer, using monochromatic Al Kα radiation (1,486.6 eV) and a low-energy flood gun as neutralizer. All X-ray photoelectron spectra were calibrated by shifting the detected carbon C 1s peak to 284.6 eV. SEM was performed on a Zeiss Supra55VP field emission scanning electron microscope with in-lens detector. The contact angles of H_2O were measured using a DSA 100 (KRUESS). ICP-OES results were collected using an Optima 8300 ICP-OES spectrometer. TEM and EDS characterizations were carried out using a FEI Titan Themis aberration-corrected transmission electron microscope at 300 kV. Brunauer–Emmett–Teller analysis was carried out using a Quantachrome Autosorb-iQ-MP/Kr BET Surface Analyzer.

XAS at the Bi L_3 edge was used to study the electronic and coordination properties of Bi samples. In situ electrochemical XAS measurements on the Bi L_3 edge were carried out at Beamline 8-ID, National Synchrotron Light Source II, Brookhaven National Laboratory, using a Si(111) monochromator and a Lytle detector. For in situ tests, continuous CO_2 flow was delivered into a homemade Teflon H cell filled with CO_2-saturated 0.5 M $KHCO_3$; a Kapton-film-covered carbon fibre paper (2D-Bi) working electrode served as the X-ray window for synchrotron radiation. Multistep potential control was used for the in situ measurements, with a hold time of ~30 min at each potential for the spectrum acquisition. Analyses of the near-edge (on an energy scale) XAS spectra were performed using Athena software.

Data availability

The data that support the plots within this paper and other findings of this study are available from the corresponding authors on reasonable request.

Received: 23 January 2019; Accepted: 2 July 2019;
Published online: 2 September 2019

References

1. Chu, S., Cui, Y. & Liu, N. The path towards sustainable energy. *Nat. Mater.* **16**, 16 (2017).
2. Lin, S. et al. Covalent organic frameworks comprising cobalt porphyrins for catalytic CO_2 reduction in water. *Science* **349**, 1208–1213 (2015).
3. Li, F., Chen, L., Knowles, G. P., MacFarlane, D. R. & Zhang, J. Hierarchical mesoporous SnO_2 nanosheets on carbon cloth: a robust and flexible electrocatalyst for CO_2 reduction with high efficiency and selectivity. *Angew. Chem. Int. Ed.* **56**, 505–509 (2017).
4. Ripatti, D. S., Veltman, T. R. & Kanan, M. W. Carbon monoxide gas diffusion electrolysis that produces concentrated C_2 products with high single-pass conversion. *Joule* **3**, 240–256 (2018).
5. Kortlever, R., Peters, I., Koper, S. & Koper, M. T. Electrochemical CO_2 reduction to formic acid at low overpotential and with high faradaic efficiency on carbon-supported bimetallic Pd-Pt nanoparticles. *ACS Catal.* **5**, 3916–3923 (2015).
6. Yang, H., Kaczur, J. J., Sajjad, S. D. & Masel, R. I. CO_2 conversion to formic acid in a three compartment cell with Sustainion™ membranes. *ECS Trans.* **77**, 1425–1431 (2017).
7. Klinkova, A. et al. Rational design of efficient palladium catalysts for electroreduction of carbon dioxide to formate. *ACS Catal.* **6**, 8115–8120 (2016).
8. Lee, W., Kim, Y. E., Youn, M. H., Jeong, S. K. & Park, K. T. Catholyte-free electrocatalytic CO_2 reduction to formate. *Angew. Chem. Int. Ed.* **57**, 6883–6887 (2018).
9. Ren, D. et al. Selective electrochemical reduction of carbon dioxide to ethylene and ethanol on copper (I) oxide catalysts. *ACS Catal.* **5**, 2814–2821 (2015).
10. Jiang, K. et al. Metal ion cycling of Cu foil for selective C-C coupling in electrochemical CO_2 reduction. *Nat. Catal.* **1**, 111 (2018).
11. Li, C. W., Ciston, J. & Kanan, M. W. Electroreduction of carbon monoxide to liquid fuel on oxide-derived nanocrystalline copper. *Nature* **508**, 504 (2014).
12. Ren, D., Wong, N. T., Handoko, A. D., Huang, Y. & Yeo, B. S. Mechanistic insights into the enhanced activity and stability of agglomerated Cu nanocrystals for the electrochemical reduction of carbon dioxide to n-propanol. *J. Phys. Chem. Lett.* **7**, 20–24 (2015).
13. Kim, D., Kley, C. S., Li, Y. & Yang, P. Copper nanoparticle ensembles for selective electroreduction of CO_2 to C_2-C_3 products. *Proc. Natl Acad. Sci. USA* **114**, 10560–10565 (2017).
14. Jouny, M., Luc, W. & Jiao, F. General techno-economic analysis of CO_2 electrolysis systems. *Ind. Eng. Chem. Res.* **57**, 2165–2177 (2018).
15. Bushuyev, O. S. et al. What should we make with CO_2 and how can we make it? *Joule* **2**, 825–832 (2018).
16. He, S. et al. The p-orbital delocalization of main-group metal boosting CO_2 electroreduction. *Angew. Chem. Int. Ed.* **57**, 16114–16119 (2018).
17. Han, N. et al. Ultrathin bismuth nanosheets from in situ topotactic transformation for selective electrocatalytic CO_2 reduction to formate. *Nat. Commun.* **9**, 1320 (2018).
18. Zheng, X. et al. Sulfur-modulated tin sites enable highly selective electrochemical reduction of CO_2 to formate. *Joule* **1**, 794–805 (2017).
19. Zhang, S., Kang, P. & Meyer, T. J. Nanostructured tin catalysts for selective electrochemical reduction of carbon dioxide to formate. *J. Am. Chem. Soc.* **136**, 1734–1737 (2014).
20. Zhong, H. et al. Bismuth nanodendrites as a high performance electrocatalyst for selective conversion of CO_2 to formate. *J. Mater. Chem. A* **4**, 13746–13753 (2016).
21. García de Arquer, F. P. et al. 2D metal oxyhalide-derived catalysts for efficient CO_2 electroreduction. *Adv. Mater.* **30**, 1802858 (2018).
22. Gao, S. et al. Partially oxidized atomic cobalt layers for carbon dioxide electroreduction to liquid fuel. *Nature* **529**, 68 (2016).

23. Manthiram, A., Yu, X. & Wang, S. Lithium battery chemistries enabled by solid-state electrolytes. *Nat. Rev. Mater.* **2**, 16103 (2017).
24. Fan, L., Wei, S., Li, S., Li, Q. & Lu, Y. Recent progress of the solid-state electrolytes for high-energy metal-based batteries. *Adv. Energy Mater.* **8**, 1702657 (2018).
25. Kuehn, C., Leder, F., Jasinski, R. & Gaunt, K. The electrolytic synthesis of hydrogen peroxide in a dual membrane cell. *J. Electrochem. Soc.* **130**, 1117–1119 (1983).
26. Yamamoto, T., Tryk, D. A., Fujishima, A. & Ohata, H. Production of syngas plus oxygen from CO_2 in a gas-diffusion electrode-based electrolytic cell. *Electrochim. Acta* **47**, 3327–3334 (2002).
27. Dinh, C.-T. et al. CO_2 electroreduction to ethylene via hydroxide-mediated copper catalysis at an abrupt interface. *Science* **360**, 783–787 (2018).
28. Jhong, H. R. M., Brushett, F. R. & Kenis, P. J. The effects of catalyst layer deposition methodology on electrode performance. *Adv. Energy Mater.* **3**, 589–599 (2013).
29. Verma, S. et al. Insights into the low overpotential electroreduction of CO_2 to CO on a supported gold catalyst in an alkaline flow electrolyzer. *ACS Energy Lett.* **3**, 193–198 (2017).
30. Weekes, D. M., Salvatore, D. A., Reyes, A., Huang, A. & Berlinguette, C. P. Electrolytic CO_2 reduction in a flow cell. *Acc. Chem. Res.* **51**, 910–918 (2018).
31. Zheng, T. et al. Large-scale and highly selective CO_2 electrocatalytic reduction on nickel single-atom catalyst. *Joule* **3**, 1–14 (2019).
32. Jiang, K. et al. Isolated Ni single atoms in graphene nanosheets for high-performance CO_2 reduction. *Energ. Environ. Sci.* **11**, 893–903 (2018).
33. Delacourt, C., Ridgway, P. L., Kerr, J. B. & Newman, J. Design of an electrochemical cell making syngas ($CO+H_2$) from CO_2 and H_2O reduction at room temperature. *J. Electrochem. Soc.* **155**, B42–B49 (2008).
34. Natsui, K., Iwakawa, H., Ikemiya, N., Nakata, K. & Einaga, Y. Stable and highly efficient electrochemical production of formic acid from carbon dioxide using diamond electrodes. *Angew. Chem. Int. Ed.* **130**, 2669–2673 (2018).
35. Min, X. & Kanan, M. W. Pd-catalyzed electrohydrogenation of carbon dioxide to formate: high mass activity at low overpotential and identification of the deactivation pathway. *J. Am. Chem. Soc.* **137**, 4701–4708 (2015).
36. Lei, F. et al. Metallic tin quantum sheets confined in graphene toward high-efficiency carbon dioxide electroreduction. *Nat. Commun.* **7**, 12697 (2016).
37. Jiang, B., Zhang, X. G., Jiang, K., Wu, D. Y. & Cai, W. B. Boosting formate production in electrocatalytic CO_2 reduction over wide potential window on Pd surfaces. *J. Am. Chem. Soc.* **140**, 2880–2889 (2018).
38. Hoffman, Z. B., Gray, T. S., Moraveck, K. B., Gunnoe, T. B. & Zangari, G. Electrochemical reduction of carbon dioxide to syngas and formate at dendritic copper-indium electrocatalysts. *ACS Catal.* **7**, 5381–5390 (2017).
39. Gao, S. et al. Ultrathin Co_3O_4 layers realizing optimized CO_2 electroreduction to formate. *Angew. Chem. Int. Ed.* **55**, 698–702 (2016).
40. Yang, H. et al. Selective CO_2 reduction on 2D mesoporous Bi nanosheets. *Adv. Energy Mater.* **8**, 1801536 (2018).
41. Zhang, Y. et al. Controllable synthesis of few-layer bismuth subcarbonate by electrochemical exfoliation for enhanced CO_2 reduction performance. *Angew. Chem. Int. Ed.* **57**, 13283–13287 (2018).
42. Zhou, Y. et al. Monolayered Bi_2WO_6 nanosheets mimicking heterojunction interface with open surfaces for photocatalysis. *Nat. Commun.* **6**, 8340 (2015).
43. Henry, N. et al. $[Bi_2O_2]^{2+}$ layers in $Bi_2O_2(OH)(NO_3)$: synthesis and structure determination. *Z. Naturforsch.* **60b**, 322–327 (2005).
44. Zhang, S. et al. Polyethylenimine-enhanced electrocatalytic reduction of CO_2 to formate at nitrogen-doped carbon nanomaterials. *J. Am. Chem. Soc.* **136**, 7845–7848 (2014).
45. Rosen, B. A. et al. Ionic liquid–mediated selective conversion of CO_2 to CO at low overpotentials. *Science* **334**, 643–644 (2011).
46. Jiang, K. et al. Transition-metal single atoms in a graphene shell as active centers for highly efficient artificial photosynthesis. *Chem* **3**, 950–960 (2017).
47. Lee, Y., Suntivich, J., May, K. J., Perry, E. E. & Shao-Horn, Y. Synthesis and activities of rutile IrO_2 and RuO_2 nanoparticles for oxygen evolution in acid and alkaline solutions. *J. Phys. Chem. Lett.* **3**, 399–404 (2012).
48. Jeong, K.-J. et al. Fuel crossover in direct formic acid fuel cells. *J. Power Sources* **168**, 119–125 (2007).
49. Kuhl, K. P., Cave, E. R., Abram, D. N. & Jaramillo, T. F. New insights into the electrochemical reduction of carbon dioxide on metallic copper surfaces. *Energ. Environ. Sci.* **5**, 7050–7059 (2012).
50. Rice, C. et al. Direct formic acid fuel cells. *J. Power Sources* **111**, 83–89 (2002).
51. Gong, M. et al. An advanced Ni-Fe layered double hydroxide electrocatalyst for water oxidation. *J. Am. Chem. Soc.* **135**, 8452–8455 (2013).
52. Vermaas, D. A., Sassenburg, M. & Smith, W. A. Photo-assisted water splitting with bipolar membrane induced pH gradients for practical solar fuel devices. *J. Mater. Chem. A* **3**, 19556–19562 (2015).
53. Masel, R. I., Liu, Z. & Sajjad, S. Anion exchange membrane electrolyzers showing 1 A/cm^2 at less than 2 V. *ECS Trans.* **75**, 1143–1146 (2016).
54. Liu, Z., Yang, H., Kutz, R. & Masel, R. I. CO_2 electrolysis to CO and O_2 at high selectivity, stability and efficiency using Sustainion membranes. *J. Electrochem. Soc.* **165**, J3371–J3377 (2018).
55. Liu, Z. et al. The effect of membrane on an alkaline water electrolyzer. *Int. J. Hydrogen Energ.* **42**, 29661–29665 (2017).
56. Millar, J., Smith, D., Marr, W. & Kressman, T. 33. Solvent-modified polymer networks. Part I. The preparation and characterisation of expanded-network and macroporous styrene–divinylbenzene copolymers and their sulphonates. *J. Chem. Soc.*, 218–225 (1963).
57. Okuhara, T., Watanabe, H., Nishimura, T., Inumaru, K. & Misono, M. Microstructure of cesium hydrogen salts of 12-tungstophosphoric acid relevant to novel acid catalysis. *Chem. Mater.* **12**, 2230–2238 (2000).
58. Bard, A. *Standard Potentials in Aqueous Solution* (Routledge, 2017).
59. Yoo, J. S., Christensen, R., Vegge, T., Nørskov, J. K. & Studt, F. Theoretical insight into the trends that guide the electrochemical reduction of carbon dioxide to formic acid. *ChemSusChem* **9**, 358–363 (2016).

Acknowledgements

This work was supported by Rice University. This research used the 8-ID (ISS) beamline of the National Synchrotron Light Source II and the Center for Functional Nanomaterials, US Department of Energy Office of Science User Facilities operated for the DOE Office of Science by Brookhaven National Laboratory under contract no. DE-SC0012704. Q.J. and H.N.A. acknowledge the support from King Abdullah University of Science and Technology (KAUST).

Author contributions

The project was conceptualized by C.X. and H.W., and supervised by H.W.; Bi-catalyst synthesis procedures were developed and performed by C.X.; C.X. and P.Z. conducted the catalytic tests and the related data processing. Materials characterization and analysis was performed by C.X. with the help of Q.J., W.L. and Y.P.; ^{1}H and ^{13}C NMR experiments and analysis were carried out by C.X. and Q.J.; in operando XAS study was performed by C.X. and H.W. with the support of E.S.; ICP-OES was conducted by Q.J.; H.N.A. provided suggestions on the work. C.X. and H.W. wrote the manuscript. All authors discussed the results and commented on the manuscript.

Competing interests

The authors declare no competing interests.

Additional information

Supplementary information is available for this paper at https://doi.org/10.1038/s41560-019-0451-x.

Reprints and permissions information is available at www.nature.com/reprints.

Correspondence and requests for materials should be addressed to H.W.

Publisher's note Springer Nature remains neutral with regard to jurisdictional claims in published maps and institutional affiliations.